Snow Thickness Estimation on First-Year Sea Ice from Late Winter Spaceborne Scatterometer Backscatter Variance

John Yackel, Torsten Geldsetzer, Mallik Mahmud, Vishnu Nandan, Stephen E. L. Howell, Randall K. Scharien and Hoi Ming Lam

February 2019

remote sensing

MDPI

Article

Snow Thickness Estimation on First-Year Sea Ice from Late Winter Spaceborne Scatterometer Backscatter Variance

John Yackel [1,*], Torsten Geldsetzer [1], Mallik Mahmud [1], Vishnu Nandan [2], Stephen E. L. Howell [3], Randall K. Scharien [2] and Hoi Ming Lam [1]

1 Department of Geography, University of Calgary, Calgary, AB T2N 1N4, Canada; geldsetz@ucalgary.ca (T.G.); msmahmud@ucalgary.ca (M.M.); hoiming.lam@ucalgary.ca (H.M.L.)
2 Department of Geography, University of Victoria, Victoria, BC V8P 5C2, Canada; vishnu@uvic.ca (V.N.); randy@uvic.ca (R.K.S.)
3 Climate Research Division, Environment and Climate Change Canada, Toronto, ON K1A 0H5, Canada; stephen.howell@canada.ca
* Correspondence: yackel@ucalgary.ca; Tel.: +1-403-220-4892

Received: 21 January 2019; Accepted: 13 February 2019; Published: 18 February 2019

Abstract: Ku- and C-band spaceborne scatterometer sigma nought (σ°) backscatter data of snow covered landfast first-year sea ice from the Canadian Arctic Archipelago are acquired during the winter season with coincident in situ snow-thickness observations. Our objective is to describe a methodological framework for estimating relative snow thickness on first-year sea ice based on the variance in σ° from daily time series ASCAT and QuikSCAT scatterometer measurements during the late winter season prior to melt onset. We first describe our theoretical basis for this approach, including assumptions and conditions under which the method is ideally suited and then present observational evidence from four independent case studies to support our hypothesis. Results suggest that the approach can provide a relative measure of snow thickness prior to σ° detected melt onset at both Ku- and C-band frequencies. We observe that, during the late winter season, a thinner snow cover displays a larger variance in daily σ° compared to a thicker snow cover on first-year sea ice. This is because for a given increase in air temperature, a thinner snow cover manifests a larger increase in basal snow layer brine volume owing to its higher thermal conductivity, a larger increase in the dielectric constant and a larger increase in σ° at both Ku- and C bands. The approach does not apply when snow thickness distributions on first-year sea ice being compared are statistically similar, indicating that similar late winter σ° variances likely indicate regions of similar snow thickness.

Keywords: snow thickness; first-year sea ice; scatterometer; backscatter (σ°) variance; ASCAT; QuikSCAT

1. Introduction

Past and state-of-the-art climate models indicate that under a warming Arctic we should expect an increase in sea ice melt during the summer months leading to a reduction in extent and thickness [1,2]. This warming Arctic, combined with melting sea ice and an increase in exposure of Arctic Ocean water, permits the increasing frequency of northward trajectory weather systems to enhance evaporation and increase the moisture flux to the atmosphere during summer and autumn [3]. There is evidence to suggest that this moist Arctic atmosphere could translate into increased meteoric snow over sea ice in the Eurasian sector [4–6] and northern Canada during early winter which would dynamically induce wintertime cooling through several large-scale atmospheric processes [7,8], and exert significant influence on atmospheric circulation patterns [9]. Conversely, some studies suggest that the snow

thickness on western Arctic sea ice has declined in recent years [10,11], largely a result of later fall freeze-up. If such trends and increased variability persist then it is possible that we could expect enhanced variability or pronounced increases/decreases in wintertime snow accumulation in certain sectors of the Arctic Ocean [12–14], thereby influencing atmosphere-sea ice-ocean exchanges and sea ice growth and decay rates. Moreover, model-based projections of summer sea ice loss in these regions may be problematic due to unrepresentative parameterizations.

There still exists considerable uncertainty in our understanding of the first-order response of the snow-sea ice system to this potential increase/decrease or change in timing in snow accumulation due to the increased variability of Arctic air temperature. Either (1) the sea ice will ablate earlier because thicker snow will reduce the equilibrium thickness of the sea ice, making it more prone to spring/summer melt; (2) increased snowfall during late winter will delay the seasonal ablation of sea ice by increasing the surface shortwave albedo; or (3) thin snow will permit thicker winter-time growth, making it more resistant to spring/summer melt [15]. To gain better understanding of these processes we require improved information on snow-thickness distributions over sea ice.

Basin-scale and pan-Arctic estimates of snow thickness on various types of sea ice have been made using passive microwave approaches [16–21]. However, satellite passive microwave-based approaches are limited by the coarse spatial resolution of state-of-the-art radiometers (e.g., ~12.5 km AMSR-2) [22,23]. NASA's Operation IceBridge (OIB) aircraft campaigns have demonstrated the capability of radar altimetry for producing snow-thickness estimates [24–30] which can be assessed against spaceborne ICESat and Cryosat-2 estimates [31]. Unfortunately, OIB datasets are acquired sporadically over space and time while satellite radar altimeter derived snow thickness estimates are subject to errors resulting from complex processes and structures within the snow cover and the choice of retracker algorithms [31–33]. The combined capability of dual-frequency radar altimeter systems, most notably Ka- and Ku-band combinations for estimating snow thickness on sea ice also shows promise [34–36]. Such methods must contend with significant uncertainties [31], but their efficacy will soon be tested once ICESat-2 data are readily available with Ka- and Ku-band radar altimeter data such as Cryosat-2 and Alti-Ka [37].

Previous synthetic aperture radar (SAR) and surface-based scatterometer studies of snow-covered FYI have provided the geophysical basis for development of active microwave based snow on sea ice thickness retrievals [38–44]. These studies have shown that changes in snow temperature on FYI are manifest as changes in total σ°. However, direct inversion of snow thickness from such changes must contend with complexities arising from competing scattering mechanisms within and below the snow volume [44,45]. These complexities are a result of varying dielectric properties which are dominated by the presence of brine primarily in the basal layer, which are a function of snow salinity, density and temperature [43,44,46–49].

An active microwave approach for estimating snow thickness that is not bound to σ° magnitudes may be more generally applicable. In this study we investigate an approach that relates the σ° variance (in dB), instead of magnitude, to snow thickness. High-resolution (5–100 m) synthetic aperture radar (SAR) data are available for developing such a methodology, however the temporal resolution and spatial coverage of SAR is typically inconsistent and incidence angle effects on σ° is an additional uncontrolled variable. Therefore, we employ spaceborne scatterometer data to determine σ° variance based on daily data, albeit at a lower, yet still improved, spatial resolution (as high as ~4.5 km).

2. Objectives and Research Design

In this work, our objective is to demonstrate a simple empirically-derived approach for estimating snow thickness on smooth, landfast FYI during the late winter season. The approach utilizes the variance in daily, scatterometer-measured σ°. We investigate both Ku- and C-band frequencies because of data availability and to take advantage of potential complementarities in how frequency-based responses to temperature induced brine volume and dielectric changes within the snow volume. We investigate FYI because we are interested in exploiting the thermodynamic-brine-dielectric effect

within the FYI snow cover [43,44] and its effect on microwave σ° [41,44]. The lack of salt in the near surface layer of multiyear sea ice prevents us from applying this methodology to this ice type. We specifically select landfast FYI to isolate different snow-thickness distributions and then assess the winter period temporal dimension of their thermodynamic and dielectric properties under variable atmospheric forcing. Since the ice is landfast, it also enables collection of time series daily and spatially coincident spaceborne scatterometer data. Smooth zones of FYI are selected so that the thermodynamically induced effect on basal brine layer snow dielectrics and microwave σ° is isolated in a manner free of scattering effects from heterogeneously distributed macroscale surface roughness or deformed ice features. Next, we describe the theoretical basis for development of our method, and in Section 4, present observational evidence from three separate case studies in the Canadian Arctic to support this approach.

From both modelling and observational perspectives, snow on FYI has been theoretically and empirically shown to affect microwave interactions either through direct scattering due to the number density and geophysical characteristics of the snow volume (e.g., density, salinity, grain microstructure), and/or indirectly through thermodynamic controls on the dielectric properties of snow (dominated by either snow wetness or brine volume) [39,43,44,50,51].

Focusing on the brine effect, snow thermodynamically modulates the snow-ice interface temperature and subsequently its dielectric properties through changes to the brine volume in the snow basal layer. These changes occur in response to diurnal fluctuations in snow temperature in response to the near surface air temperature during late winter when no melting occurs. Thicker snow will insulate the basal snow layer from air temperature changes keeping the brine volume and dielectric properties constant. Thin snow is more thermally diffusive and will manifest a larger change in brine volume and dielectric constant and subsequent microwave σ°. The association in relative quantity between snow thickness as a function of changing air and snow temperature has been firmly established [43,44,48–52] and assessed with spaceborne SAR data [38,53–55].

Our hypothesis, stemming from previous research, is that thinner snow covers on smooth, thick (> ~160 cm) FYI manifests a larger variance (at the daily time scale) in spaceborne microwave σ° for a given natural evolution of surface air temperature change (at the daily time scale), in late winter prior to melt onset (MO). This is because the basal snow layer brine volume will respond to this air temperature forcing more rapidly at diurnal and daily timescales and with greater change for a thin snow cover compared to a thicker, greater insulating snow cover, owing to the higher (lower) thermal conductivity, respectively. As a result, the dielectric properties will also manifest a correspondingly larger (smaller) change and directly affect the amount of surface and/or volume scattering from the snow/ice system.

Two assumptions are required. First, we consider the ice surface roughness constant and consistent during our wintertime σ° observations, and secondly, that any snowfall accumulation occurring during the measurement period is uniform across each of the case study regions. In the first instance, each of the case study sites is expected to have its own microscale ice roughness characteristics within a scatterometer resolution cell of 4.45 km. We specifically chose sites locations of different, but homogeneous ice surface roughness (from a SAR σ° perspective) because we hypothesize that they would capture differing amounts of blowing snow over the course of the winter season. Therefore, each of the case study sites has different absolute (i.e., baseline) wintertime σ°, as a function of surface roughness, scatterometer frequency and incidence angle. Given the landfast nature of the sea ice in our study, we do not expect any significant change in ice surface roughness towards changes in surface or volume scattering contributions to the total σ° throughout the winter season.

3. Damping Effect

Given that the primary driver of basal snow layer brine volume changes is snow temperature, σ° variability is expected to be related to air temperature variability. If air temperature variance is low then snow temperature variance, and associated σ° variance, are thus also expected to be low,

irrespective of snow thickness. To normalize for differences in air temperature variance between cases, we relate it to the σ° variance (calculated in dB):

$$\zeta = \sqrt{\frac{s^2 Ta}{s^2 \sigma^0}} \quad (1)$$

where *Ta* is the daily mean air temperature over the study period. Both *Ta* and σ° are detrended using a first-order linear regression prior to calculation of their variances. The resulting measure, ζ, termed the damping effect, is an indication of the ability of the snow cover to moderate the air temperature variance. This is directly related to the thermal conductivity of the snow cover [15]; as the damping effect increases, the thermal conductivity decreases. Therefore, the damping effect is expected to be related to the snow thickness under the assumption of uniform snow density between sites.

4. Methods

4.1. Case Studies

Data were collected from three previous field studies, hereafter referred to as case studies (Figure 1). The first and second case studies come from the 2007/08—Circumpolar Flaw Lead System Study (CFL) located in Franklin Bay (hereafter denoted as FB), Northwest Territories, Canada [56]. (Figure 2a). The third and fourth case studies are from the 2014 Arctic Science Partnership Ice Covered Ecosystems–CAMbridge bay Process Studies (ICE-CAMPS) and the 2018 Polar Knowledge Canada funded field campaigns, located in Dease Strait near Cambridge Bay (hereafter denoted as CB) Nunavut (Figure 2b,c). We select three sample locations within the Franklin Bay 2008 (FB08) and Cambridge Bay 2014 (CB14) case studies to represent thin (<13 cm), medium (>13 cm <23 cm) and thick (>23 cm) snow thickness classes; these provide disparate and relative measures of snow thickness. Similarly, three sample locations, of different absolute σ° resulting from different microscale ice roughness, are selected within the Cambridge Bay 2018 (CB18) case study. Site selection within each case study was largely determined from pre-planning and analysis of RADARSAT-1 and 2 and Sentinel 1A/B SAR imagery whereby sites were chosen based on their size and homogeneity of σ° within a spaceborne scatterometer resolution cell (i.e., 4.45 km).

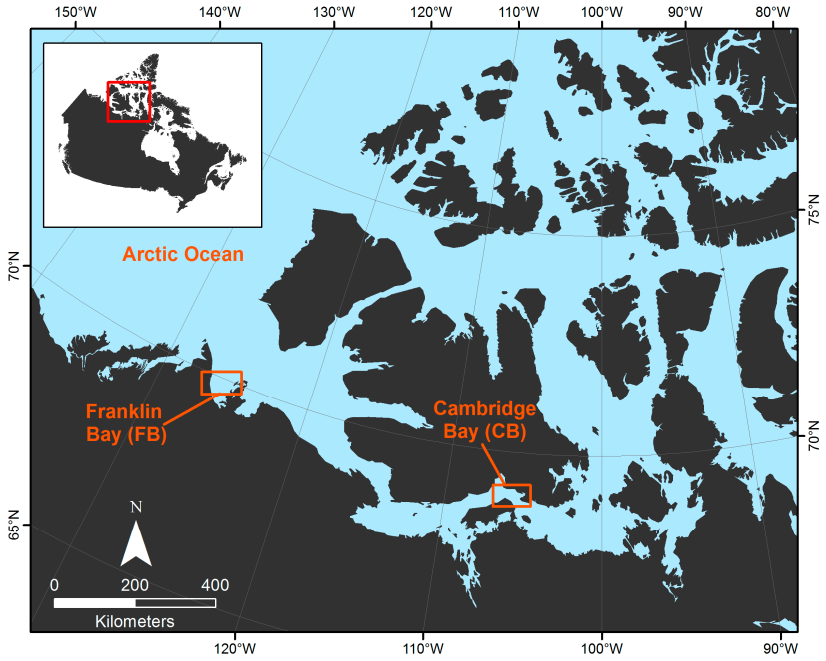

Figure 1. Franklin Bay [2008] and Cambridge Bay [2014 and 2018] case study locations on landfast first-year sea ice in the western Canadian Arctic Archipelago.

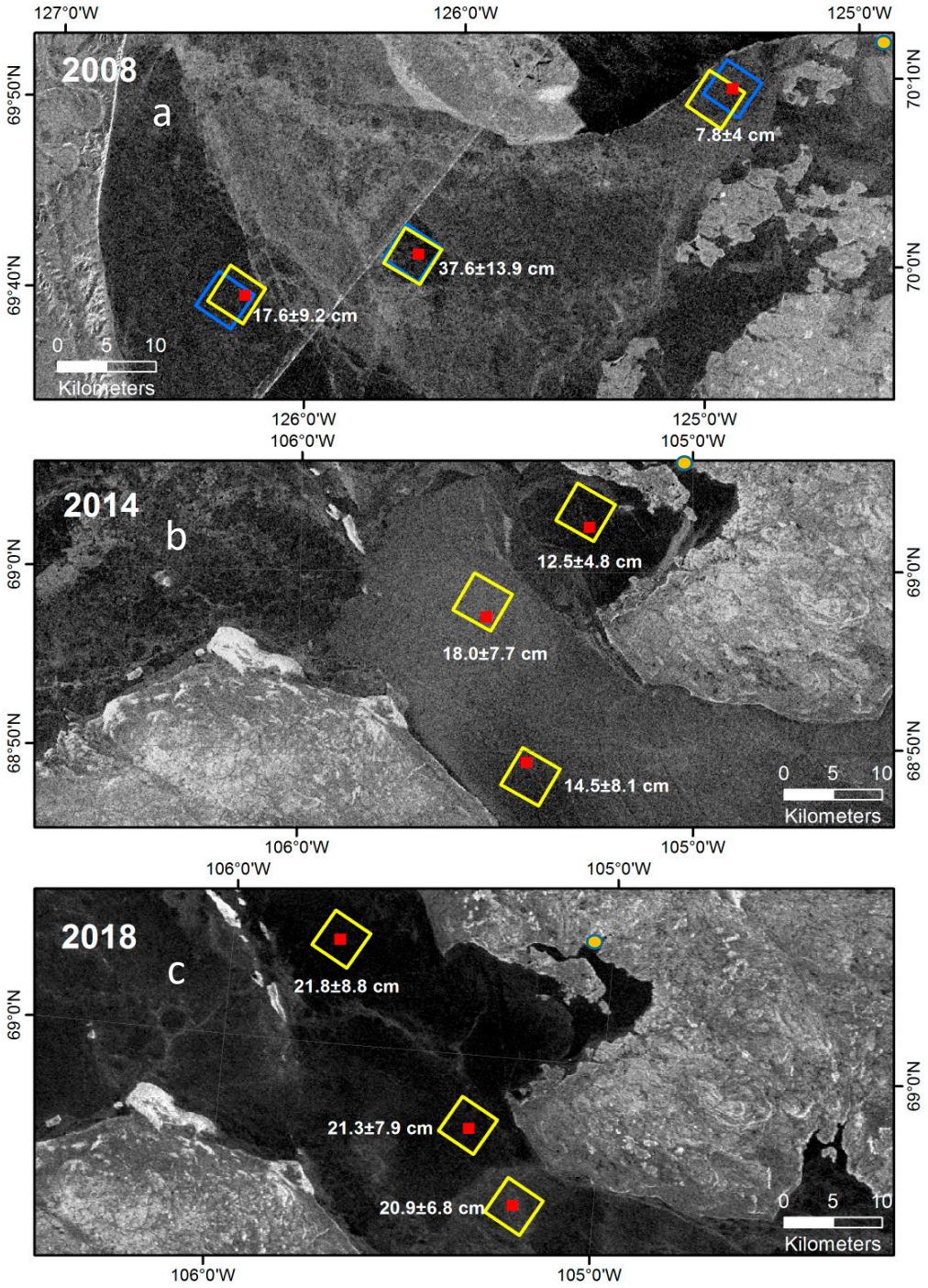

Figure 2. RADARSAT-1 (**a**) and RADARSAT-2 (**b**,**c**) winter season synthetic aperture radar (SAR) images showing Franklin Bay, 2008 (**a**), Dease Strait near Cambridge Bay, 2014 (**b**) and 2018 (**c**) snow covered sea ice case study sites. In situ mean and standard deviation of snow thickness transect locations are indicated by the red squares inside the QuikSCAT/ASCAT (see Section 4.3) (**a**) and ASCAT (**b**,**c**) 4.45 km ASCAT scatterometer sample locations (yellow squares) and QuikSCAT (blue squares). Note the tonal homogeneity within each of the yellow and blue squares.

4.2. Snow and Ice Thickness Measurements

Due to logistical constraints including limited helicopter time and low air temperatures during sampling, snow-thickness data at each study site were acquired while walking in an 'L' shape of two intersecting linear transects, parallel, and orthogonal, to the prevailing snow drift pattern. This was

done to capture the wind influence on snow redistribution and to ensure representative statistics are captured [57]. For the case studies, the three separate measurement locations were sampled on the same day (FB08) or within 2 or 3 days (CB14 and CB18) via helicopter or snowmobile. The snow thickness transects were acquired on April 17 via helicopter for FB08, April 23-25 via snow machine for CB14, and May 17–19 via snow machine for CB18. A digital Magnaprobe snow depth probe [58] was used to sample snow thickness. Sampling was conducted at 1 m intervals and data have a vertical accuracy of 0.5 cm. Figure 2 shows the mean and standard deviation of the snow thickness transects at each of the sampling locations.

The sea ice thickness in FB was measured by drill hole and found to be 180 $\pm$ 3 cm throughout the study period of FB08 [59]. Ice thickness was repeatedly measured at 185 $\pm$ 5cm at the 13 cm site at CB14. The sea ice thickness throughout the study period for the CB18 sites was repeatedly measured at 166 $\pm$ 16 cm.

4.3. Spaceborne Scatterometer Data

We use satellite σ° data from Quik Scatterometer (QuikSCAT) and the Advanced Scatterometer (ASCAT). QuikSCAT operates at Ku-band (13.4 GHz) frequency and linear horizontal (H) and vertical (V) transmit-receive polarization combinations (HH and VV). ASCAT operates at C-band (5.26 GHz) frequency and VV polarization. In this study, we utilize the "all passes" scatterometer image reconstruction (SIR) products from the Scatterometer Climate Record Pathfinder (SCP) dataset available at http://scp.byu.edu. This enhanced resolution SIR product increases the spatial resolution from ~25 km to 4.45 km [60]. The SIR products provide a 1-day temporal resolution σ° for QuikSCAT normalized to 54° incidence angle for VV polarization and 46° for HH polarization and 2-day temporal resolution σ° normalized to a 40° for ASCAT. We observed a 5-day cycle in the time series winter σ° data, previously identified by [61], which is caused by inappropriate application of incidence angle dependencies. We apply a variant of the adjustment made in [61], whereby the SCP normalization process is first reversed to provide the original σ° (a')

$$a' = a - b(40 - j) \tag{2}$$

where, a is the SCP-normalized σ° (to 40°), j is the mean daily incidence angle, and b is the daily-varying incidence angle slope that was applied. a' is then normalized to 49° using a consistent incidence angle slope (b') to provide the adjusted σ° (σ^0_{adj})

$$\sigma^0_{adj} = a' + b'(49 - j) \tag{3}$$

where, b' is -0.22 dB/°, from [62] for FYI. The mean incidence angle for our case studies is ~49°; therefore, we normalize to 49° to minimize the slope adjustment required.

4.4. Meteorological Data

Air temperature and precipitation data corresponding to the case studies were obtained from both the on-ice installed micro-meteorological station and the nearest Environment and Climate Change Canada (ECCC) meteorological station. Air temperature data for the FB case study are obtained from the Cape Parry ECCC station (15 to 50 km from sites), and precipitation (not available at Cape Parry) from the Paulatuk ECCC station (90 km from snow thickness sites). Air temperature data for the CB case studies were obtained from the on-ice meteorological station (2 to 20 km from sites), and precipitation from the Cambridge Bay ECCC station (10 to 30 km from snow thickness sites). These data are recorded hourly with daily means presented (Figure 3. Our assumption is that the daily air temperature at each of the three sample sites within a case study is statistically similar given the proximity of the sites (tens of kilometers) in relation to the larger scale (hundreds of kilometers) air mass and synoptic systems governing daily average air temperature.

Although we are aware that various components of the surface radiation balance (i.e., longwave and net all-wave fluxes) can impact the dielectric properties of the snow cover on FYI [42,43,49,50] we are only able to assess the bulk sensible heat flux effects (i.e., air temperature) in this work. As such, we hereafter refer to 'air temperature' as the principal atmospheric forcing agent of changes to snow brine volume and in turn its dielectric properties.

4.5. Identifying Winter to Melt Onset (MO) Transition

We arbitrarily begin our analysis of the case studies on April 1 in the corresponding year. At this stage, the FYI at our study sites for all case studies is both (1) thick (>160 cm) and (2) landfast (stationary). Therefore, the thick FYI (>160 cm) acts to minimize the ocean to ice-surface heat flux to the point that it is negligible compared to the surface forcing with respect to affecting the brine volume in the basal layer of the snow during the winter season [44].

Hourly air temperatures are used to identify and validate the likely date of snow MO, and to identify brief warming periods that approach the freezing mark prior to MO. MO on snow covered FYI is found on the day when the mean air temperature of 3 consecutive days (from one day before to one day after), for the first time, exceeds −0.44 °C [63]. From a time series microwave σ° perspective, MO can be identified as the first major σ° upturn from stable winter σ° values [64,65]. This most often occurs several days earlier than an air temperature identified date of MO on FYI because basal snow layer brine volume and associated dielectric constant increases are sufficiently high at snow-ice interface temperatures of ~−5 °C to initiate a detectable increase in microwave σ° [66,67]. For the FB08 case study, a 42-day period ending the day before MO is selected for analysis (1 April 2008 to 12 May 2008) (Figure 3a). A 53-day period ending the day before MO is selected for analysis (1 April 2014 to 23 May 2014) for CB14. For CB18 case study, 66 days (1 April 2018 to 5 June 2018) are assessed (Figure 3c).

5. Results

The time series evolution of the daily air temperature and meteoric snow and/or rain at our FB08 case study is illustrated in Figure 3a. Air temperature at FB08 on April 1 was near −30 °C and gradually warmed to the freezing mark for the first time on May 14. Significant snow fell early in the study period. The time series evolution of the daily air temperature and meteoric snow and/or rain at the CB14 site is illustrated in Figure 3b. Air temperature at CB14 on April 1 was ~−35 °C and steadily warmed over the course of the next six weeks. There were two occasions in CB14 when the air temperature briefly exceeded the freezing mark for several hours (max of 1.6 °C on 14 May 2014 and 0.4 °C on 18 May 2014), but the daily mean was still below freezing in both cases, at −3.4 °C and −1.5 °C, respectively (Figure 3b). Air temperature quickly resumed to winter conditions thereafter in both cases. As such, the daily resolution σ°does not reflect these short warming events owing to the low thermal diffusivity of the snow over such time scales. CB14 also received a significant snowfall event 12-hours prior to our scatterometer detected MO date on May 24 but its influence of changing MO appears negligible. The winter to MO transition was typical of the Canadian Arctic Archipelago for these two locations. The time series evolution of the daily air temperature and meteoric snow and/or rain at our CB18 site is illustrated in Figure 3c. The air temperature at CB18 site on April 1 was ~−21 °C and steadily increased to 0 °C on June 6, when MO was detected for all ASCAT sites. There were few snowfall events over the course of the late winter season. The MO date for CB18 was ~2–3 weeks later than the FB08 and CB14 sites.

The time series evolution of the air temperature along with each of the daily QuikSCAT σ° time series acquisitions for the three FB08 case study snow thickness sites is illustrated in Figure 4. The rapid upturn in σ° for all three sites beginning on 13 May 2008 denotes MO and is indicated by the vertical dashed line. Although the 'baseline' (absolute σ°) varies between sites, of relevance here is the variance in the daily winter time series σ° as a function of snow thickness. As shown in Table 1 and Figure 4, the site with the thinnest snow cover (mean = ~8 cm) corresponds to the largest winter σ° variance

(red line in Figures 4–7) whereas the site with the thickest snow cover (mean = ~38 cm; green line) corresponds to the smallest winter σ° variance. Figure 5 illustrates the time series evolution of the air temperature alongside each of the daily ASCAT σ° time series acquisitions for the FB08 case study. As with QuikSCAT, the ASCAT series exhibits the same greater variance for thinner snow covers. Figure 6 illustrates the time series evolution of the air temperature alongside each of the daily ASCAT σ° time series acquisitions for the CB14 case study. Again, as shown in Table 1 and Figure 6 (green line), the site with the thinnest snow cover (mean = 12.5 cm) corresponds to the largest winter σ° variance (red line) whereas the thickest snow cover (mean = 18 cm) corresponds to the smallest winter σ° variance. The time series evolution of the air temperature alongside each of the daily ASCAT σ° time series acquisitions for the CB18 case study is illustrated in Figure 7. Each of the three sites at CB18 had very similar snow thickness distributions (both mean and standard deviation). Similarly, the difference in ASCAT winter σ° variance between the three sites is visually indistinguishable in the time series (Figure 7; Table 1).

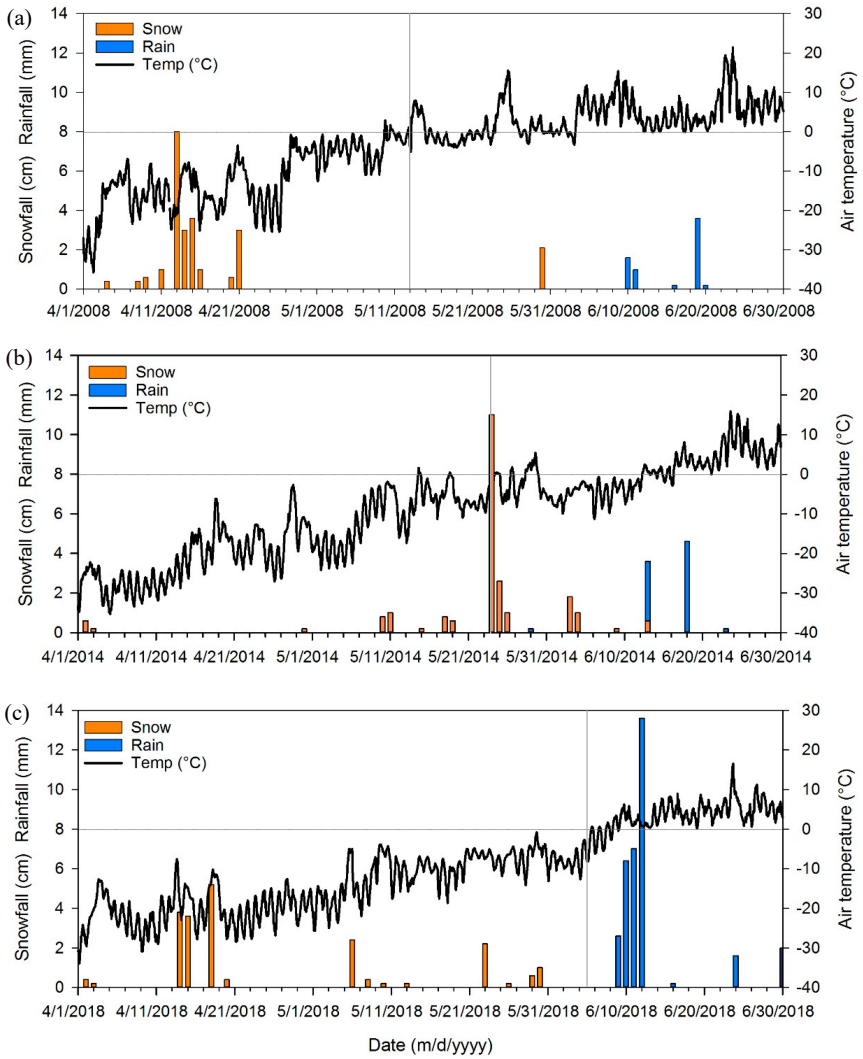

Figure 3. Hourly air temperature and daily precipitation total for Franklin Bay, 2008 (measured at Cape Parry Environment and Climate Change station) (**a**), Cambridge Bay, 2014 (measured at Cambridge Bay EEEC station) (**b**) and 2018 (**c**) (measured at the on-ice station). Thin horizontal and vertical grey lines correspond to the freezing mark and date of melt onset (MO), respectively.

Table 1. Ku- and C-band scatterometer data used in case studies along with mean snow thickness, snow thickness standard deviation, snow thickness sample size, σ° variance prior to melt onset and number of daily winter σ° observations in time series.

	ASCAT 2008 Franklin Bay, Canada			**QuikSCAT 2008 Franklin Bay, Canada**			**ASCAT 2014 Cambridge Bay, Canada**			**ASCAT 2018 Cambridge Bay, Canada**		
	C-Band/VV-pol/normalized to 49°/daily all-passes product			Ku-Band/VV-pol/54°/AM-pass			C-Band/VV-pol/normalized to 49°/daily all-passes product			C-Band/VV-pol/normalized to 49°/daily all-passes product		
Site	Mean snow thickness (cm) (sample size)	Snow thickness std. dev (cm)	variance of σ° prior to MO (dB^2)	Mean snow thickness (cm) (sample size)	Snow thickness std. dev (cm)	variance of σ° prior to MO (dB^2)	Mean snow thickness (cm) (sample size)	Snow thickness std. dev (cm)	variance of σ° prior to MO (dB^2)	Mean snow thickness (cm) (sample size)	Snow thickness std. dev (cm)	variance of σ° prior to MO (dB^2)
1	7.8 (n = 145)	4.0	0.67 (n = 43)	7.8 (n = 14)	4.0	1.35 (n = 41)	12.5 (n = 400)	4.8	0.29 (n = 52)	20.9 (n = 734)	6.8	0.34 (n = 66)
2	17.6 (n = 204)	9.2	0.32 (n = 43)	17.6 (n = 20)	9.2	0.33 (n = 41)	14.5 (n = 400)	8.1	0.18 (n = 52)	21.3 (n = 1368)	7.9	0.26 (n = 66)
3	37.6 (n = 203)	13.9	0.03 (n = 43)	37.6 (n = 203)	13.9	0.18 (n = 41)	18.0 (n = 400)	7.7	0.11 (n = 52)	21.8 (n = 1043)	8.8	0.33 (n = 66)

Table 2. Inter-site assessment of statistically significant differences of snow thickness and winter σ° variance. Site numbers are as in Table 1. Snow thickness is assessed using Welch's t-test, σ° variance is assessed using an F-test. Both are two-tailed, assessed at 95% confidence level.

	ASCAT 2008 Franklin Bay, Canada	**QuikSCAT 2008 Franklin Bay, Canada**	**ASCAT 2014 Cambridge Bay, Canada**	**ASCAT 2018 Cambridge Bay, Canada**
	C-Band/VV-pol/normalized to 49°/daily all-passes product	Ku-Band/VV-pol/54°/AM-pass	C-Band/VV-pol/normalized to 49°/daily all-passes product	C-Band/VV-pol/normalized to 49°/daily all-passes product
Snow thickness (cm)	$1 \neq 2 \neq 3 \neq 1$	$1 \neq 2 \neq 3 \neq 1$	$1 \neq 2 \neq 3 \neq 1$	$1 \approx 2 \approx 3 \neq 1$
Variance of σ° prior to MO (dB^2)	$1 \neq 2 \neq 3 \neq 1$	$1 \neq 2 \approx 3 \neq 1$	$1 \approx 2 \approx 3 \neq 1$	$1 \approx 2 \approx 3 \approx 1$

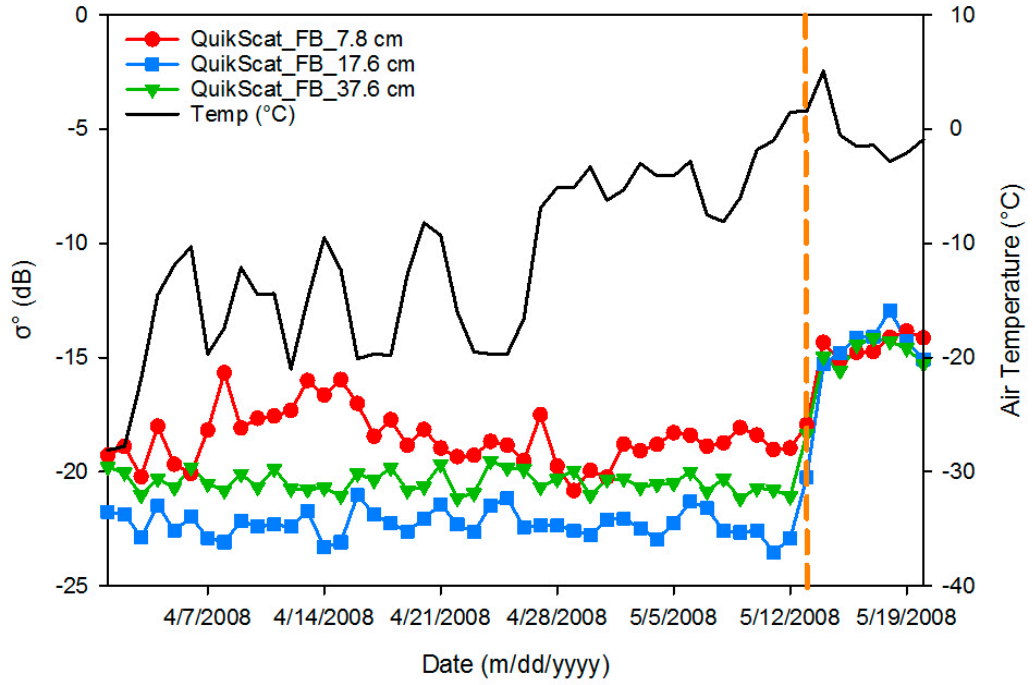

Figure 4. Time series evolution of daily mean air temperature and QuikSCAT σ° for the Franklin Bay (FB) snow thickness sites between 1 April and 20 May 2008 (during the winter season). The upturn in σ° at melt onset on ~13 May for each of the snow thickness sites is denoted by the vertical dashed line.

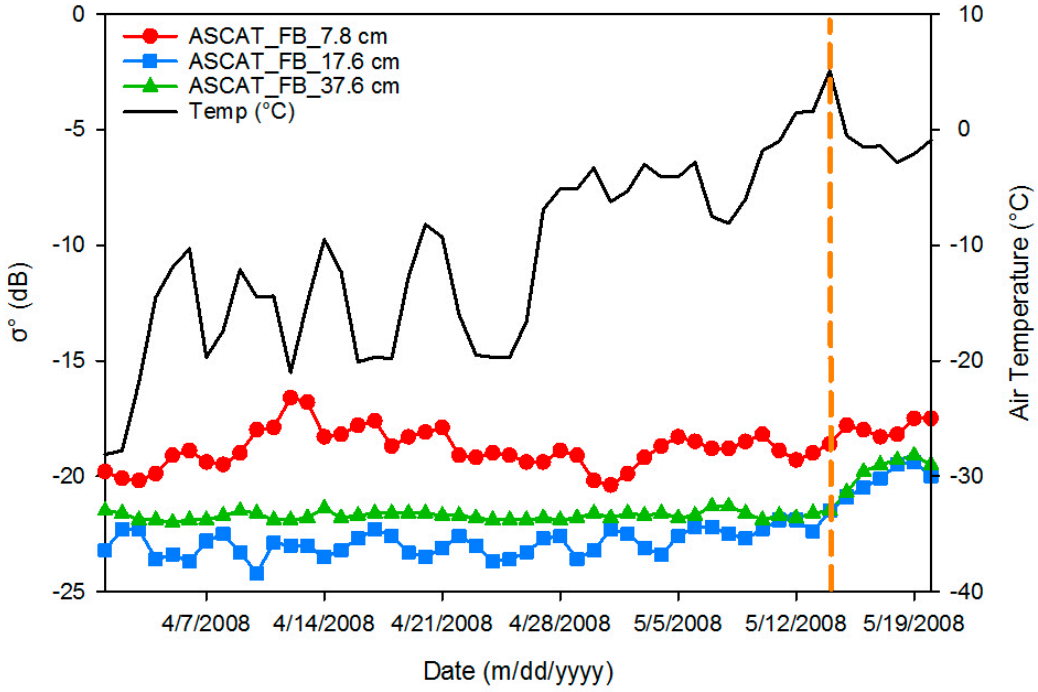

Figure 5. Time series evolution of daily mean air temperature and ASCAT σ° for the Franklin Bay (FB) snow thickness sites between 1 April and 20 May 2008 (during the winter season). The upturn in σ° at melt onset on ~14 May for each of the snow thickness sites is denoted by the vertical dashed line.

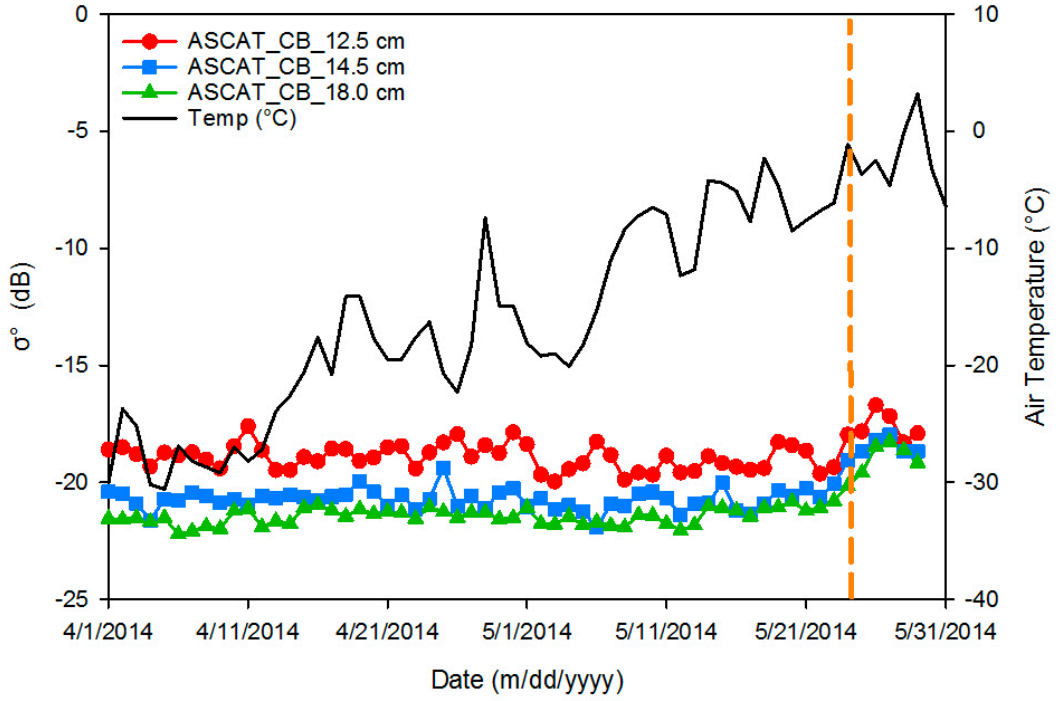

Figure 6. Time series evolution of daily mean air temperature and ASCAT σ° for the Cambridge Bay (CB) snow thickness sites between 1 April and 28 May 2014 (during the winter season). The upturn in σ° at melt onset on ~24 May for each of the snow thickness sites is denoted by the vertical dashed line.

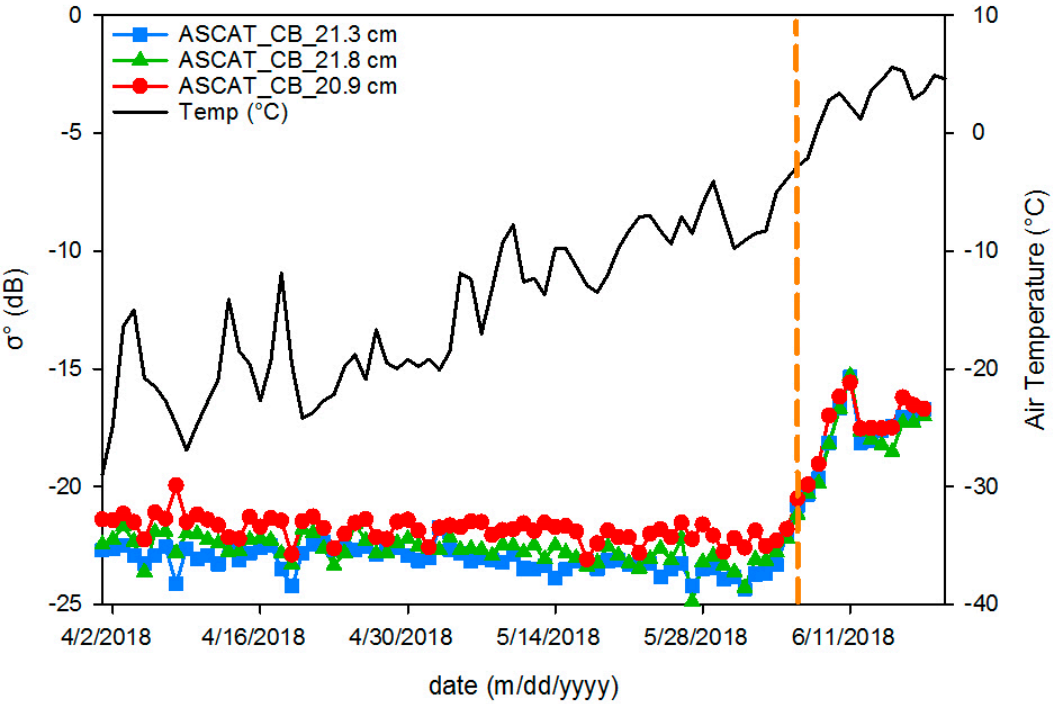

Figure 7. Time series evolution of daily mean air temperature and ASCAT σ° for the Cambridge Bay (CB) snow thickness sites between 1 April and 15 June 2018 (during the winter season). The upturn in ASCAT σ° at melt onset on ~5 June for each of the snow thickness sites is denoted by the vertical dashed line.

For the FB08 case study, the range of snow thickness between the three sites is largest (7.8 to 37.6 cm), as is the σ° variance (0.67 to 0.03 dB^2), whereas the small snow-thickness range for CB14 sites (12.5 to 18.0 cm) manifests to a smaller range of σ° variances (0.29 to 0.11 dB^2).

Results from a test of significant difference of snow thickness means for all sites, using the two-tailed Welch's t-test ($\alpha = 0.05$) given that the variances and the number of samples are unequal, are shown in Table 2. Mean snow thickness for FB08 sites are statistically different, as are the CB14 ones. For CB18, only Sites 1 and 3 are statistically different. Results from a two-tailed F-test ratio ($\alpha = 0.05$) to assess the statistical difference of σ° variances are illustrated in Table 2. The σ° data are normally distributed according to a Kolmogorov-Smirnov test, meeting the requirement for an F-test. For FB08, the QuikSCAT σ° variance is different between Sites 1 and 2, and between 1 and 3, but not between 2 and 3. This suggests that, for Ku-band, damping effect of the 9.8 cm difference between Sites 1 and 2 is sufficient to moderate the thermal response of the basal snow layers, and that the additional 20 cm difference between Sites 2 and 3 provide no additional moderating influence. In contrast, all three FB08 sites exhibit statistically different σ° variances at C-band. This may be the result of the greater penetration depth of C-band relative to Ku-band, and thus additional volume scattering contributions from the basal layers. For CB14, only Sites 1 and 3 exhibit statistically different σ° variances. This suggests that a minimum snow thickness difference is required to resolve the variance differences; 5.5 cm in this case. This is supported by the results for CB18, where the differences in snow thickness are too small to produce statistically different σ° variances.

To assess the damping effect, we plot it against the absolute snow thickness (Figure 8). The standard error was found to be 4.82 with an adjusted R^2 of 0.67 ($p = 0.0045$). We limit this analysis to the ASCAT samples to avoid the frequency differences. We find a somewhat weak, but significant, relationship between the damping effect and snow thickness, as expected. The lack of data points constrains our ability to develop a model or draw robust conclusions; however, based on an initial case study analysis, the variance of σ°, when related to the variance of air temperature, may yield skill in estimating snow thickness.

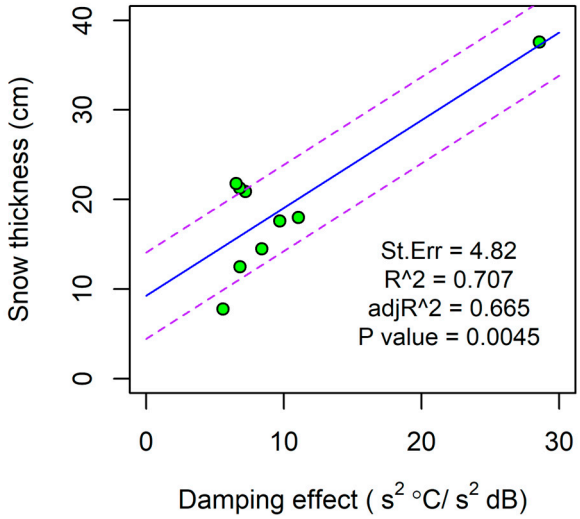

Figure 8. Damping effect versus snow thickness for all ASCAT samples. The blue line is a linear regression and the dashed purple lines represent the standard error of the regression.

6. Discussion

One important factor to consider in these results is the increased sensitivity of higher frequency microwaves with snow covered FYI. This is observed in the case of higher frequency Ku-band QuikSCAT observations when compared to the lower frequency C-band ASCAT data from FB08. Previous research has demonstrated that the microwave σ° response is more sensitive and larger at

higher frequencies owing to the dielectric property changes as a function of frequency for consistent thermodynamic forcing over similar snow thickness on FYI [39,49,51,68,69].

The overall σ° from scatterometers are a combination of surface and volume scattering mechanisms resulting from snow thermo-physical properties of snow [44], snow redistribution [57] to adjusting within and between site snow thickness and ice surface roughness. These factors are not measured in detail in this study, therefore we are unable to evaluate their partial contribution to the overall σ°. These processes limit our skill at explaining inter-site differences of snow thickness and winter σ° variance (Table 2).

The results from the first three case studies support our stated hypothesis that a thinner snow cover manifests a larger fluctuation in basal snow layer brine volume and dielectric permittivity resulting in a larger fluctuation in σ°, compared to thicker snow covers, under variable but similar atmospheric forcing during late winter. The fourth case study demonstrates that statistically indistinguishable snow-thickness distributions would likewise reflect statistically similar variances in winter σ° prior to MO.

We surmise that snow-covered sea ice with a winter daily time series of σ° (at either Ku- or C-band) that is more variable relative to another nearby location will have a statistically thinner snow cover under the assumption's framework described. Given that acquiring snow-thickness data on sea ice is logistically challenging in winter, we are limited to assessing distributions from only these four specific case studies with three sites each. Additional case study sites over large spatial scales are needed to fully validate this approach.

7. Conclusions

The objectives of this paper were to present a simple empirically-derived approach for estimating relative snow thickness on smooth, landfast FYI, based on the variance in daily measured spaceborne Ku- and C-band microwave σ° during the late winter season prior to MO. We investigate both Ku- and C-band frequencies for their ability to do so primarily because of spaceborne scatterometer data availability. We investigate only the FYI type because we are interested in exploiting the thermodynamic-brine-dielectric effect within the snow cover and its effect on microwave σ°. The lack of salt in the near surface layer of MYI prevents us from investigating snow thickness over this ice type using this theory. We specifically select landfast FYI for measurement because we are interested in assessing how a locations snow-thickness distribution modulates the thermodynamic and dielectric properties of the snow cover over the course of the winter season and how this can be detected by spaceborne scatterometer measurements.

To accomplish this objective, we reviewed the thermodynamic controls of snow-covered FYI towards modulating the dielectric properties of this volume and subsequent influence on microwave scattering at both Ku- and C-band. Results demonstrate, for the four cases presented, that for a given air temperature evolution during the winter season prior to MO, the thinner snow cover sites permit the associated natural air temperature fluctuations from both radiative and synoptic forcing to manifest larger changes to the brine volume fraction and dielectric constant within the snow cover through the effect of its higher thermal conductivity. This results in greater variability in thermodynamically induced σ° changes as detected by spaceborne active scatterometers at both Ku- or C-band. Conversely, a thicker snow cover acts to dampen a given winter air temperature change towards altering the basal snow layer temperature and thereby producing a smaller change in the bulk snow brine volume and dielectric constant and leads to reduced σ° variance. We also presented a case study for snow-thickness locations which had statistically similar means, the variance of the daily winter σ° prior to MO was also statistically similar thereby demonstrating a likely situation when the methodology cannot be applied. The application of the snow thickness-temperature-brine-dielectric-microwave σ° theory illustrated through these case studies demonstrates that it may be possible to estimate the relative thickness of snow on landfast FYI in the late winter season prior to MO. Future research should attempt to address

the larger scale applicability of this method using spaceborne scatterometer data and relate it to other estimates of snow thickness on sea ice from either passive microwave or data fusion products.

Author Contributions: J.Y., and T.G. designed the experiment. J.Y. and T.G. formulated the research methodology and wrote the manuscript. T.G., M.M. and V.N. provided necessary data and contributed to manuscript development and proof reading. T.G., M.M., V.N., S.E.L.H., R.K.S. and H.M.L. contributed with additional inputs during manuscript development and proof reading.

Funding: This research was funded by Canadian NSERC Discovery grants to John Yackel and Randy Scharien as well as Polar Continental Shelf Project and Polar Knowledge Canada support to C.J. Mundy, Brent Else, Randy Scharien and John Yackel. The APC was funded by Canadian NSERC Discovery grants to John Yackel.

Acknowledgments: The authors would like to thank the participants of the CFL-IPY 2007-08, Arctic-ICE 2012 and Cambridge Bay 2018 field experiments based out of Franklin Bay, NU and Resolute Bay, Nunavut, Canada. We would like to thank all team members for their support and hard work in the field programs, including Principal Investigators, D.G. Barber and C.J. Mundy (CEOS, University of Manitoba) and B. Else (University of Calgary). We extend our sincere thanks to the Polar Continental Shelf Project and MEOPAR (Marine Environmental Observation Prediction and Response Network) for their funding and logistical support. We also thank the crew of the CCGS Amundsen for helicopter support in 2008. We acknowledge Canadian NSERC Discovery and Tools and Infrastructure grants to R. Scharien and J. Yackel towards this work. The Canadian Ice Service support in providing, planning and ordering RADARSAT-2 imagery is appreciated. Supplementary RADARSAT-2 imagery and planning support was provided by the Canadian Space Agency's Science and Operational Applications Research program. RADARSAT-2 Data and Products © MacDonald, Dettwiler and Associates Ltd. 2012. All Rights Reserved. RADARSAT is an official mark of the Canadian Space Agency.

Conflicts of Interest: The authors declare no conflicts of interest.

References

1. Wang, M.; Overland, J.E. A Sea Ice Free Summer Arctic within 30 Years: An Update from CMIP5 Models. *Geophys. Res. Lett.* **2012**, *39*. [CrossRef]
2. Laliberté, F.; Howell, S.E.L.; Kushner, P.J. Regional Variability of a Projected Sea Ice-Free Arctic during the Summer Months. *Geophys. Res. Lett.* **2016**, *43*, 256–263. [CrossRef]
3. Mortin, J.; Svensson, G.; Graversen, R.G.; Kapsch, M.-L.; Stroeve, J.C.; Boisvert, L.N. Melt Onset over Arctic Sea Ice Controlled by Atmospheric Moisture Transport. *Geophys. Res. Lett.* **2016**, *43*, 6636–6642. [CrossRef]
4. Granskog, M.A.; Rösel, A.; Dodd, P.A.; Divine, D.; Gerland, S.; Martma, T.; Leng, M.J. Snow Contribution to First-year and Second-year Arctic Sea Ice Mass Balance North of Svalbard. *J. Geophys. Res. Ocean.* **2017**, *122*, 2539–2549. [CrossRef]
5. Merkouriadi, I.; Cheng, B.; Graham, R.M.; Rösel, A.; Granskog, M.A. Critical Role of Snow on Sea Ice Growth in the Atlantic Sector of the Arctic Ocean. *Geophys. Res. Lett.* **2017**, *44*, 10479–10485. [CrossRef]
6. Rösel, A.; Itkin, P.; King, J.; Divine, D.; Wang, C.; Granskog, M.A.; Krumpen, T.; Gerland, S. Thin Sea Ice, Thick Snow, and Widespread Negative Freeboard Observed During N-ICE2015 North of Svalbard. *J. Geophys. Res. Ocean.* **2018**, *123*, 1156–1176. [CrossRef]
7. Liu, J.; Curry, J.A.; Wang, H.; Song, M.; Horton, R.M. Impact of Declining Arctic Sea Ice on Winter Snowfall. *Proc. Natl. Acad. Sci. USA* **2012**, *109*, 4074–4079. [CrossRef] [PubMed]
8. Cohen, J.L.; Furtado, J.C.; Barlow, M.A.; Alexeev, V.A.; Cherry, J.E. Arctic Warming, Increasing Snow Cover and Widespread Boreal Winter Cooling. *Environ. Res. Lett.* **2012**, *7*, 014007. [CrossRef]
9. Cassano, E.N.; Cassano, J.J.; Higgins, M.E.; Serreze, M.C. Atmospheric Impacts of an Arctic Sea Ice Minimum as Seen in the Community Atmosphere Model. *Int. J. Climatol.* **2014**, *34*, 766–779. [CrossRef]
10. Hezel, P.J.; Zhang, X.; Bitz, C.M.; Kelly, B.P.; Massonnet, F. Projected Decline in Spring Snow Depth on Arctic Sea Ice Caused by Progressively Later Autumn Open Ocean Freeze-up This Century. *Geophys. Res. Lett.* **2012**, *39*, L17505. [CrossRef]
11. Webster, M.A.; Rigor, I.G.; Nghiem, S.V.; Kurtz, N.T.; Farrell, S.L.; Perovich, D.K.; Sturm, M. Interdecadal Changes in Snow Depth on Arctic Sea Ice. *J. Geophys. Res. Ocean.* **2014**, *119*, 5395–5406. [CrossRef]
12. Boisvert, L.N.; Stroeve, J.C. The Arctic Is Becoming Warmer and Wetter as Revealed by the Atmospheric Infrared Sounder. *Geophys. Res. Lett.* **2015**, *42*, 4439–4446. [CrossRef]

13. Boisvert, L.N.; Webster, M.A.; Petty, A.A.; Markus, T.; Bromwich, D.H.; Cullather, R.I.; Boisvert, L.N.; Webster, M.A.; Petty, A.A.; Markus, T.; Bromwich, D.H.; Cullather, R.I. Intercomparison of Precipitation Estimates over the Arctic Ocean and Its Peripheral Seas from Reanalyses. *J. Clim.* **2018**, *31*, 8441–8462. [CrossRef]
14. Blanchard-Wrigglesworth, E.; Webster, M.A.; Farrell, S.L.; Bitz, C.M. Reconstruction of Snow on Arctic Sea Ice. *J. Geophys. Res. Ocean.* **2018**, *123*, 3588–3602. [CrossRef]
15. Sturm, M.; Perovich, D.K.; Holmgren, J. Thermal Conductivity and Heat Transfer through the Snow on the Ice of the Beaufort Sea. *J. Geophys. Res.* **2002**, *107*. [CrossRef]
16. Comiso, J.C.; Cavalieri, D.J.; Markus, T. Sea Ice Concentration, Ice Temperature, and Snow Depth Using AMSR-E Data. *IEEE Trans. Geosci. Remote Sens.* **2003**, *41*, 243–252. [CrossRef]
17. Powell, D.C.; Markus, T.; Cavalieri, D.J.; Gasiewski, A.J.; Klein, M.; Maslanik, J.A.; Stroeve, J.C.; Sturm, M. Microwave Signatures of Snow on Sea Ice: Modeling. *IEEE Trans. Geosci. Remote Sens.* **2006**, *44*, 3091–3102. [CrossRef]
18. Markus, T.; Powell, D.C.; Wang, J.R. Sensitivity of Passive Microwave Snow Depth Retrievals to Weather Effects and Snow Evolution. *IEEE Trans. Geosci. Remote Sens.* **2006**, *44*, 68–77. [CrossRef]
19. Brucker, L.; Markus, T. Arctic-Scale Assessment of Satellite Passive Microwave-Derived Snow Depth on Sea Ice Using Operation IceBridge Airborne Data. *J. Geophys. Res. Ocean.* **2013**, *118*, 2892–2905. [CrossRef]
20. Maaß, N.; Kaleschke, L.; Tian-Kunze, X.; Drusch, M. Snow Thickness Retrieval over Thick Arctic Sea Ice Using SMOS Satellite Data. *Cryosph.* **2013**, *7*, 1971–1989. [CrossRef]
21. Rostosky, P.; Spreen, G.; Farrell, S.L.; Frost, T.; Heygster, G.; Melsheimer, C. Snow Depth Retrieval on Arctic Sea Ice From Passive Microwave Radiometers-Improvements and Extensions to Multiyear Ice Using Lower Frequencies. *J. Geophys. Res. Ocean.* **2018**, *123*, 7120–7138. [CrossRef]
22. Drobot, S.D.; Barber, D.G. Towards Development of a Snow Water Equivalence (SWE) Algorithm Using Microwave Radiometry over Snow Covered First-Year Sea Ice. *Photogramm. Eng. Remote Sens.* **1998**, *64*, 415–423.
23. Langlois, A.; Barber, D.G. Passive Microwave Remote Sensing of Seasonal Snow-Covered Sea Ice. *Prog. Phys. Geogr.* **2007**, *31*, 539–573. [CrossRef]
24. Kurtz, N.T.; Farrell, S.L. Large-Scale Surveys of Snow Depth on Arctic Sea Ice from Operation IceBridge. *Geophys. Res. Lett.* **2011**, *38*. [CrossRef]
25. Kwok, R.; Panzer, B.; Leuschen, C.; Pang, S.; Markus, T.; Holt, B.; Gogineni, S. Airborne Surveys of Snow Depth over Arctic Sea Ice. *J. Geophys. Res.* **2011**, *116*, C11018. [CrossRef]
26. Kwok, R.; Cunningham, G.F.; Manizade, S.S.; Krabill, W.B. Arctic Sea Ice Freeboard from IceBridge Acquisitions in 2009: Estimates and Comparisons with ICESat. *J. Geophys. Res. Ocean.* **2012**, *117*, C02018. [CrossRef]
27. Farrell, S.L.; Kurtz, N.; Connor, L.N.; Elder, B.C.; Leuschen, C.; Markus, T.; McAdoo, D.C.; Panzer, B.; Richter-Menge, J.; Sonntag, J.G. A First Assessment of IceBridge Snow and Ice Thickness Data Over Arctic Sea Ice. *IEEE Trans. Geosci. Remote Sens.* **2012**, *50*, 2098–2111. [CrossRef]
28. Kwok, R. Simulated Effects of a Snow Layer on Retrieval of CryoSat-2 Sea Ice Freeboard. *Geophys. Res. Lett.* **2014**, *41*, 5014–5020. [CrossRef]
29. Newman, T.; Farrell, S.L.; Richter-Menge, J.; Connor, L.N.; Kurtz, N.T.; Elder, B.C.; McAdoo, D. Assessment of Radar-Derived Snow Depth over Arctic Sea Ice. *J. Geophys. Res. Ocean.* **2014**, *119*, 8578–8602. [CrossRef]
30. Kwok, R.; Kurtz, N.T.; Brucker, L.; Ivanoff, A.; Newman, T.; Farrell, S.L.; King, J.; Howell, S.; Webster, M.A.; Paden, J.; et al. Intercomparison of Snow Depth Retrievals over Arctic Sea Ice from Radar Data Acquired by Operation IceBridge. *Cryosphere* **2017**, *11*, 2571–2593. [CrossRef]
31. Kwok, R.; Kacimi, S. Three Years of Sea Ice Freeboard, Snow Depth, and Ice Thickness of the Weddell Sea from Operation IceBridge and CryoSat-2. *Cryosphere* **2018**, *12*, 2789–2801. [CrossRef]
32. Ricker, R.; Hendricks, S.; Helm, V.; Skourup, H.; Davidson, M. Sensitivity of CryoSat-2 Arctic Sea-Ice Freeboard and Thickness on Radar-Waveform Interpretation. *Cryosph.* **2014**, *8*, 1607–1622. [CrossRef]
33. Ricker, R.; Hendricks, S.; Perovich, D.K.; Helm, V.; Gerdes, R. Impact of Snow Accumulation on CryoSat-2 Range Retrievals over Arctic Sea Ice: An Observational Approach with Buoy Data. *Geophys. Res. Lett.* **2015**, *42*, 4447–4455. [CrossRef]
34. Lawrence, I.R.; Tsamados, M.C.; Stroeve, J.C.; Armitage, T.W.K.; Ridout, A.L. Estimating Snow Depth over Arctic Sea Ice from Calibrated Dual-Frequency Radar Freeboards. *Cryosph.* **2018**, *12*, 3551–3564. [CrossRef]

35. Guerreiro, K.; Fleury, S.; Zakharova, E.; Rémy, F.; Kouraev, A. Potential for Estimation of Snow Depth on Arctic Sea Ice from CryoSat-2 and SARAL/AltiKa Missions. *Remote Sens. Environ.* **2016**, *186*, 339–349. [CrossRef]
36. Armitage, T.W.K.; Ridout, A.L. Arctic Sea Ice Freeboard from AltiKa and Comparison with CryoSat-2 and Operation IceBridge. *Geophys. Res. Lett.* **2015**, *42*, 6724–6731. [CrossRef]
37. Kwok, R.; Markus, T. Potential Basin-Scale Estimates of Arctic Snow Depth with Sea Ice Freeboards from CryoSat-2 and ICESat-2: An Exploratory Analysis. *Adv. Sp. Res.* **2018**, *62*, 1243–1250. [CrossRef]
38. Gill, J.P.S.; Yackel, J.J.; Geldsetzer, T.; Fuller, M.C. Sensitivity of C-Band Synthetic Aperture Radar Polarimetric Parameters to Snow Thickness over Landfast Smooth First-Year Sea Ice. *Remote Sens. Environ.* **2015**, *166*, 34–49. [CrossRef]
39. Nandan, V.; Geldsetzer, T.; Islam, T.; Yackel, J.J.; Gill, J.P.S.; Fuller, M.C.; Gunn, G.; Duguay, C. Ku-, X- and C-Band Measured and Modeled Microwave Backscatter from a Highly Saline Snow Cover on First-Year Sea Ice. *Remote Sens. Environ.* **2016**, *187*, 62–75. [CrossRef]
40. Nandan, V.; Geldsetzer, T.; Mahmud, M.; Yackel, J.; Fuller, M.C.; Gill, J.P.S.; Ramjan, S. Ku-, X-, and C-band Microwave Backscatter Indices from Saline Snow Covers on Arctic First-Year Sea Ice. *Remote Sens.* **2017**, *9*, 757. [CrossRef]
41. Yackel, J.J.; Barber, D.G. Observations of Snow Water Equivalent Change on Landfast First-Year Sea Ice in Winter Using Synthetic Aperture Radar Data. *IEEE Trans. Geosci. Remote Sens.* **2007**, *45*, 1005–1015. [CrossRef]
42. Barber, D.G.; Thomas, A. The Influence of Cloud Cover on the Radiation Budget, Physical Properties, and Microwave Scattering Coefficient (°) of First-Year and Multiyear Sea Ice. *IEEE Trans. Geosci. Remote Sens.* **1998**, *36*, 38–50. [CrossRef]
43. Barber, D.G.; Fung, A.K.; Grenfell, T.C.; Nghiem, S.V.; Onstott, R.G.; Lytle, V.I.; Perovich, D.K.; Gow, A.J. The Role of Snow on Microwave Emission and Scattering over First-Year Sea Ice. *IEEE Trans. Geosci. Remote Sens.* **1998**, *36*, 1750–1763. [CrossRef]
44. Barber, D.G.; Nghiem, S.V. The Role of Snow on the Thermal Dependence of Microwave Backscatter over Sea Ice. *J. Geophys. Res. Ocean.* **1999**, *104*, 25789–25803. [CrossRef]
45. Fuller, M.C.; Geldsetzer, T.; Gill, J.P.S.; Yackel, J.J.; Derksen, C. C-Band Backscatter from a Complexly-Layered Snow Cover on First-Year Sea Ice. *Hydrol. Process.* **2014**, *28*, 4614–4625. [CrossRef]
46. Drinkwater, M.R.; Crocker, G.B. Modelling Changes in Scattering Properties of the Dielectric and Young Snow-Covered Sea Ice at GHz Requencies. *J. Glaciol.* **1988**, *34*, 274–282. [CrossRef]
47. Geldsetzer, T.; Mead, J.B.; Yackel, J.J.; Scharien, R.K.; Howell, S.E.L. Surface-Based Polarimetric C-Band Scatterometer for Field Measurements of Sea Ice. *IEEE Trans. Geosci. Remote Sens.* **2007**, *45*, 3405–3416. [CrossRef]
48. Geldsetzer, T.; Langlois, A.; Yackel, J. Dielectric Properties of Brine-Wetted Snow on First-Year Sea Ice. *Cold Reg. Sci. Technol.* **2009**, *58*, 47–56. [CrossRef]
49. Nandan, V.; Scharien, R.; Geldsetzer, T.; Mahmud, M.; Yackel, J.J.; Islam, T.; Gill, J.P.S.; Fuller, M.C.; Gunn, G.; Duguay, C. Geophysical and Atmospheric Controls on Ku-, X- and C-Band Backscatter Evolution from a Saline Snow Cover on First-Year Sea Ice from Late-Winter to Pre-Early Melt. *Remote Sens. Environ.* **2017**, *198*, 425–441. [CrossRef]
50. Nandan, V.; Geldsetzer, T.; Yackel, J.J.; Islam, T.; Gill, J.P.S.; Mahmud, M. Multifrequency Microwave Backscatter from a Highly Saline Snow Cover on Smooth First-Year Sea Ice: First-Order Theoretical Modeling. *IEEE Trans. Geosci. Remote Sens.* **2017**, *55*, 2177–2190. [CrossRef]
51. Barber, D.G.; Reddan, S.P.; LeDrew, E.F. Statistical Characterization of the Geophysical and Electrical Properties of Snow on Landfast First-Year Sea Ice. *J. Geophys. Res.* **1995**, *100*, 2673–2686. [CrossRef]
52. Yackel, J.J.; Gill, J.P.S.; Geldsetzer, T.; Fuller, M.C.; Nandan, V. Diurnal Scale Controls on C-Band Microwave Backscatter From Snow-Covered First-Year Sea Ice During the Transition From Late Winter to Early Melt. *IEEE Trans. Geosci. Remote Sens.* **2017**, *55*, 3860–3874. [CrossRef]
53. Yackel, J.J.; Barber, D.G.; Papakyriakou, T.N.; Breneman, C. First-Year Sea Ice Spring Melt Transitions in the Canadian Arctic Archipelago from Time-Series Synthetic Aperture Radar Data, 1992–2002. *Hydrol. Process.* **2007**, *21*, 253–265. [CrossRef]
54. Hanesiak, J.M.; Yackel, J.J.; Barber, D.G. Effect of Melt Ponds on First-Year Sea Ice Ablation – Integration of Radarsat-I and Thermodynamic Modelling. *Can. J. Remote Sens.* **2001**, *27*, 433–442. [CrossRef]

55. Iacozza, J.; Barber, D.G. An Examination of Snow Redistribution over Smooth Land-Fast Sea Ice. *Hydrol. Process.* **2010**, *24*, 850–865. [CrossRef]
56. Sturm, M.; Holmgren, J. An Automatic Snow Depth Probe for Field Validation Campaigns. *Water Resour. Res.* **2018**, *54*, 9695–9701. [CrossRef]
57. Garneau, M.-È.; Roy, S.; Lovejoy, C.; Gratton, Y.; Vincent, W.F. Seasonal Dynamics of Bacterial Biomass and Production in a Coastal Arctic Ecosystem: Franklin Bay, Western Canadian Arctic. *J. Geophys. Res.* **2008**, *113*, C07S91. [CrossRef]
58. Early, D.S.; Long, D.G. Image Reconstruction and Enhanced Resolution Imaging from Irregular Samples. *IEEE Trans. Geosci. Remote Sens.* **2001**, *39*, 291–302. [CrossRef]
59. Zheng, J.; Geldsetzer, T.; Yackel, J. Snow Thickness Estimation on First-Year Sea Ice Using Microwave and Optical Remote Sensing with Melt Modelling. *Remote Sens. Environ.* **2017**, *199*, 321–332. [CrossRef]
60. Mahmud, M.S.; Geldsetzer, T.; Howell, S.E.L.; Yackel, J.J.; Nandan, V.; Scharien, R.K. Incidence Angle Dependence of HH-Polarized C- and L-Band Wintertime Backscatter Over Arctic Sea Ice. *IEEE Trans. Geosci. Remote Sens.* **2018**, *56*, 6686–6698. [CrossRef]
61. Mahmud, M.S.; Howell, S.E.L.; Geldsetzer, T.; Yackel, J. Detection of Melt Onset over the Northern Canadian Arctic Archipelago Sea Ice from RADARSAT, 1997–2014. *Remote Sens. Environ.* **2016**, *178*, 59–69. [CrossRef]
62. Livingstone, C.; Onstott, R.; Arsenault, L.; Gray, A.; Singh, K. Microwave Sea-Ice Signatures near the Onset of Melt. *IEEE Trans. Geosci. Remote Sens.* **1987**, *GE-25*, 174–187. [CrossRef]
63. Barber, D.G.; Papakyriakou, T.N.; LeDrew, E.F. On the Relationship between Energy Fluxes, Dielectric Properties, and Microwave Scattering over Snow Covered First-Year Sea Ice during the Spring Transition Period. *J. Geophys. Res.* **1994**, *99*, 22401–22411. [CrossRef]
64. Yackel, J.J.; Barber, D.G.; Papakyriakou, T.N. On the Estimation of Spring Melt in the North Water Polynya Using RADARSAT-1. *Atmos. Ocean* **2001**, *39*, 195–208. [CrossRef]
65. Ulaby, F.T.; Stiles, W.H.; Abdelrazik, M. Snowcover Influence on Backscattering from Terrain. *IEEE Trans. Geosci. Remote Sens.* **1984**, *GE-22*, 126–133. [CrossRef]
66. Drinkwater, M.R. LIMEX '87 Ice Surface Characteristics: Implications for C-Band SAR Backscatter Signatures. *IEEE Trans. Geosci. Remote Sens.* **1989**, *27*, 501–513. [CrossRef]
67. Kendra, J.R.; Sarabandi, K.; Ulaby, F.T. Radar Measurements of Snow: Experiment and Analysis. *IEEE Trans. Geosci. Remote Sens.* **1998**, *36*, 864–879. [CrossRef]
68. Dierking, W.; Dall, J. Sea-Ice Deformation State from Synthetic Aperture Radar Imagery - Part I: Comparison of C- and L-B and and Different Polarization. *In IEEE Transactions on Geoscience and Remote Sens.* **2007**, *45*, 3610–3621. [CrossRef]
69. Paul, S.; Willmes, S.; Hoppmann, M.; Hunkeler, P.A.; Wesche, C.; Nicolaus, M.; Heinemann, G.; Timmermann, R. The impact of early-summer snow properties on Antartctic landfast sea-ice X-band backscatter. *Ann. Glacio.* **2015**, *56*, 263–273. [CrossRef]